
Artificial Neural Network Algorithm for Pulse Shape Discrimination in $2\pi\alpha$ and $2\pi\beta$ Particle Surface Emission Rate Measurements

Yuan-Qiao Li¹, Bao-Ji Zhu^{1,2}, Yang Lv¹, Heng Zhu^{1,2}, Min Lin^{1,2}, Ke-Sheng Chen^{1,2},
Li-Jun Xu^{1,2}

¹China Institute of Atomic Energy, Beijing 102413, China

²National Key Laboratory for Metrology and Calibration Techniques, Beijing 102413, China

lisi03@foxmail.com

Abstract To enhance the accuracy of $2\pi\alpha$ and $2\pi\beta$ particle surface emission rate measurements and address the identification issues of nuclides in conventional methods, this study introduces two artificial neural network (ANN) algorithms: back propagation (BP) and genetic algorithm-based back propagation (GA-BP). These algorithms classify pulse signals from distinct α and β particles. Their discrimination efficacy is assessed by simulating standard pulse signals and those produced by contaminated sources, mixing α and β particles within the detector. This study initially showcases energy spectrum measurement outcomes, subsequently tests the ANNs on the measurement and validation datasets, and contrasts the pulse shape discrimination efficacy of both algorithms. Experimental findings reveal that the proportional counter's energy resolution is not ideal, thus rendering energy analysis insufficient for distinguishing between $2\pi\alpha$ and $2\pi\beta$ particles. The BP neural network realizes approximately 99% accuracy for $2\pi\alpha$ particles and approximately 95% for $2\pi\beta$ particles, thus surpassing the GA-BP's performance. Additionally, the results suggest enhancing β particle discrimination accuracy by increasing the digital acquisition card's threshold lower limit. This study offers an advanced solution for the $2\pi\alpha$ and $2\pi\beta$ surface emission rate measurement method, presenting superior adaptability and scalability over conventional techniques.

Keywords Pulse shape discrimination; Artificial neural networks; Alpha and beta sources; Multi-wire proportional counter; Surface emission rate.

1. Introduction

According to international and Chinese standards ^[1–4], α and β plane sources are essential for calibrating, verifying, and ensuring the stability of radioactivity measurement and surface contamination monitoring instruments. In international comparisons ^[5], most institutions utilize a gas-flow 2π multi-wire proportional counter as the detector for $2\pi\alpha$ and $2\pi\beta$ particle measurements, offering a detection efficiency of almost 100% for these particles. However, owing to the multi-wire proportional counter's low energy resolution, discriminating between particles becomes challenging. Some institutions ^[6–8] continue using the single-channel pulse amplitude analysis method for counting, which measures pulse amplitude but fails to discriminate the pulse shapes of varying radio-nuclides. With the rapid advancement of digital signal acquisition technology, some establishments ^[9] have realized plane-source spectrum measurements. Nonetheless, owing to varying plane source preparation processes, uncertainty regarding the spectral consistency of the same radionuclide exists. Moreover, for contaminated detectors or mixed plane sources

infused with other radio-nuclides, the conventional 2π multi-wire proportional counter cannot identify radioactive particles or assess plane source purity. Historically, α and β particle discrimination necessitated a blend of energy, time, and frequency analysis techniques. This poses challenges when measuring beta particles in a detector contaminated by alpha particles. The increased operating voltage results in the ionization effect of alpha particles to enter the limited proportional region. Consequently, the collected ionization number N does not align proportionally with the initial total ionization N_0 , thereby leading to a spike in detector counts. Thus, enhancing the accuracy of $2\pi\alpha$ and $2\pi\beta$ surface emission rate measurements demands effective particle discrimination.

Various particle-identification models have been developed over the past four decades. Pulse shape discrimination (PSD) techniques can be classified into three main categories: time domain, frequency domain, and machine learning. These methods are listed in Table 1.

Table 1 Classification of particle pulse shape discrimination techniques

Classification	Time-domain features	Frequency-domain features	Machine learning
Specific methods	Rise time	Frequency domain pulse gradient	Artificial neural network
	Charge comparison	Wavelet analysis	Fuzzy C-means clustering
	Pulse gradient	/	/

Discrimination techniques for particles based on time- or frequency-domain attributes and fuzzy C-mean clustering^[10] utilize limited features of the pulse shape for classification. Such methods may overlook other significant pulse signal features. Although they exhibit effective discrimination, these techniques consume significant processing time for multi-particle classification, thus compromising efficiency. The artificial neural network (ANN) approach offers automatic learning and parameter adjustment capabilities, thus reducing labor and time expenditure. This method can expand the radio-nuclide classification with fresh training data, thus enhancing system scalability and adaptability.

ANNs have been employed for nuclear pulse shape analysis^[11,12]; however, initial applications were constrained by inadequate computational power, limited input parameters, few training samples, and a low ADC sampling rate. Over the past decade, ANN methodologies have evolved, finding successful application in γ particle-specific activity measurements^[13], α/γ identification^[14], n/γ pulse shape discrimination^[15–19], γ -energy spectrum analysis^[20–22], and pulse shape repair^[23–26]. However, most studies focused on semiconductor and scintillator detectors, with ANNs not yet applied to $2\pi\alpha$ and $2\pi\beta$ particle surface emission rate measurements.

The objective of the current study is to introduce two ANN algorithms for the discrimination of $2\pi\alpha$ and $2\pi\beta$ particles. Neural network methods are employed to distinguish pulse signals adulterated by non-standard ionized particles within a simulated environment, considering the detector's dual standard-voltage operational states. The study examines the viability of this technique for surface emission rate measurement systems reliant on 2π multi-wire proportional counters. Furthermore, it discusses the efficacy of different neural network architectures and algorithmic parameters. The study initially details the experimental setup, training dataset, and

validation set. Subsequently, it elucidates the characteristics of the two ANNs and offers an in-depth overview of their application. Finally, the findings derived from the experimental data concerning both ANNs are presented.

2. Experimental set-up

2.1 Data acquisition methods

In this study, the detector employed was a large-area 2π multi-wire proportional counter^[27], a product of the China Institute of Atomic Energy (CIAE). The detector operates at voltages of 2100 V for α sources and 2800 V for β sources. It boasts a counting response uniformity exceeding $\pm 0.4\%$, an effective detection area of approximately 1400 cm², short-term stability measurements surpassing 0.3% over 8 h, and long-term stability measurements surpassing 0.8% over a year. A schematic of the 2π multi-wire proportional counter system used in this study is shown in Figure 1. The counter utilized P-10 gas for counting, composed of 90% Ar and 10% CH₄. The gas flow rate was consistently held at 20–60 mL/min during the detector's routine operation. All sources deployed in the experiments were calibrated, with their traces leading back to the $2\pi\alpha$ and $2\pi\beta$ surface emission rate standard devices at CIAE. To align the count rate recorded by the digital acquisition card with the plane sources' surface emission rate, the acquisition card's pulse amplitude trigger threshold was adjusted during the surface emission rate calibration experiments. For configuring the acquisition card, a fixed sampling length was determined based on the pulse's maximum width. A pertinent starting point for sampling was selected. Amplitude and time resolutions were fine-tuned to prevent signal saturation and to ensure comprehensive pulse signal capture across all plane source varieties. Each signal sample spanned 1048 ns, with a time step of 1 ns, and it was divided into 1048 equidistant components. This type of configurations implied that minimal saturation or signal pile-up was observed throughout data collection. The digital acquisition card was then primed to yield an energy spectrum, which is elaborated in Section 4.1.

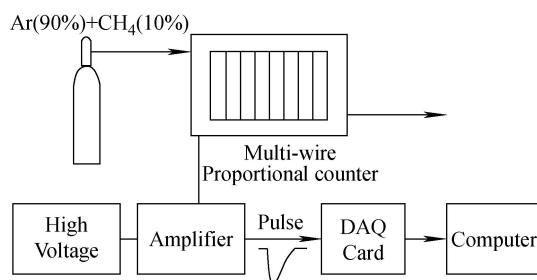


Fig. 1 Block diagram for pulse signal acquisition for large area flow-through 2π multi-wire proportional counter

2.2 Training and verification datasets

In this study, two α plane sources (^{238}Pu and ^{241}Am) and two β plane sources (^{204}Tl and ^{90}Sr) were employed for the experiments. The chosen α -sources, ^{241}Am and ^{238}Pu , are prominent in 2π surface emission rate measurements owing to their high purity relative to other α -plane sources. Additionally, the high-energy β -sources, ^{204}Tl and ^{90}Sr , were selected to minimize noise interference and to facilitate neural network training with broader and more pronounced pulse shapes for effective classification. Six distinct sets of pulse measurements were acquired, with each set comprising

signals from a sole radiation source. Four of these sets captured measurements of $2\pi\alpha$ and $2\pi\beta$ surface emission rates under standard conditions. The remaining two sets simulated signals contaminated by extraneous particles. To represent particle discrimination and surface emission rate measurements in real-world scenarios, the data were categorized into a $2\pi\alpha$ measurement dataset and $2\pi\beta$ measurement dataset. The $2\pi\alpha$ measurement dataset encompassed α_1 , α_2 , and α_3 . Specifically, α_1 and α_2 correspond to pulse shapes obtained from the detector for ^{238}Pu and ^{241}Am , both at a direct current (DC) voltage of 2100 V. Whereas α_3 contains pulse shape data from the ^{204}Tl source, also at 2100 V DC, simulating the pulse data acquired during β particle contamination in $2\pi\alpha$ surface emission rate measurements. The $2\pi\beta$ measurement dataset encompassed β_1 , β_2 , and β_3 . The β_1 and β_2 subsets contain pulse shapes from the detector for ^{204}Tl and ^{90}Sr , measured at a DC voltage of 2800 V. Whereas the β_3 subset contains pulse shape data from the ^{241}Am source at 2800 V DC, emulating the pulse data influenced by α particle contamination in $2\pi\beta$ surface emission rate measurements.

Table 1 $2\pi\alpha$ experimental dataset

Dataset	Nuclides	Operating voltage (V)	Total number	Training set number	Validation set number	Description
α_1	^{238}Pu	2100	10000	7500	2500	Normal operation
α_2	^{241}Am	2100	10000	7500	2500	Normal operation
α_3	^{204}Tl	2100	6000	4500	1500	β contamination during $2\pi\alpha$ measurement

Table 2 $2\pi\beta$ experimental dataset

Dataset	Nuclides	Operating voltage (V)	Total number	Training set number	Validation set number	Description
β_1	^{204}Tl	2800	10000	7500	2500	Normal operation
β_2	^{90}Sr	2800	10000	7500	2500	Normal operation
β_3	^{241}Am	2800	10000	7500	2500	α contamination during $2\pi\beta$ measurement

The ^{204}Tl source was consistent in α_3 and β_1 datasets, whereas the ^{241}Am source was utilized in α_2 and β_3 sets. The pulse sample count for the α_3 dataset was limited. This was because the ^{204}Tl operated at a DC voltage of 2100 V, falling beneath the ionization threshold. Hence, the mostly signal captured was the detector's background signal.

3. Artificial neural network

The structure of the artificial neural network consists of an input layer, a hidden layer, and an output layer, as illustrated in Figure 2. In this structure, "x" represents the input signal. Each neuron within the network receives input signals from preceding neurons. These signals traverse connections characterized by weights (w_1 , w_2) and biases (b_1 , b_2). The neuron then aggregates these to derive a total input value. Subsequently, this value is compared with the neuron's threshold value and processed through an activation function. The resultant output is forwarded as input to neurons in the subsequent layers.

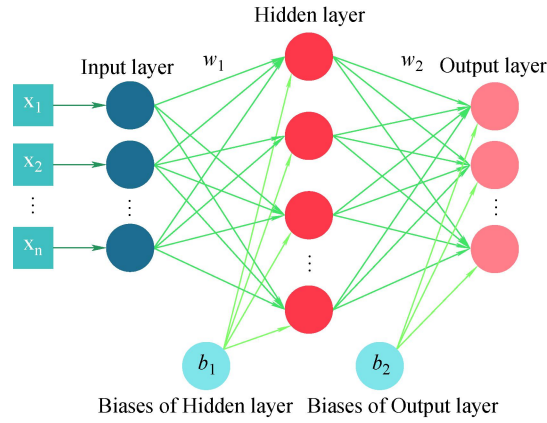


Fig. 2 Typical structural model of a neural network

This study applied two different neural network algorithms for $2\pi\alpha$ and $2\pi\beta$ pulse shape classification prediction: back propagation (BP) and genetic algorithm-based back propagation (GA-BP). This section describes the principles, network structures, and parameters of the algorithms. Both algorithms were implemented in MATLAB (MathWorks, Natick, MA, USA). The computational hardware for the BP neural network comprised a CPU (Intel i5-12400F) with 16 GB of RAM, and that for the GA-BP neural network comprised a CPU (Intel i9-12900K) with 16 GB of RAM.

3.1 BP neural network

3.1.1 Principle

A BP neural network serves as the fundamental element of a feed-forward network. With its straightforward architecture, numerous tunable parameters, and robust operability, it stands as the most prevalent and advanced training algorithm. The neural network's design encompasses the count of neurons in the input, hidden, and output layers. Initial training parameters encompass the learning rate, maximum iteration count, number of validation failures, inter-layer activation functions, evaluation function, and its minimal value. The error, which is the discrepancy between the output layer's outcome and actual result matching the input data, is the back-propagated information. With each forward and backward propagation, the neural network updates its parameters. Training entails repeated forward and backward propagations, which refine their parameters to approximate a genuine relationship. In theory, a sufficiently layered and node-equipped network can approximate any nonlinear functional relationship.

3.1.2 Network structure and parameters

The same BP neural network was trained on two datasets: $2\pi\alpha$ and $2\pi\beta$. Each dataset encompassed three pulse types (α_1, α_2 , and α_3 for $2\pi\alpha$ and β_1, β_2 , and β_3 for $2\pi\beta$). The network featured 1048 input neurons, correlating with the amplitude vector of a singular pulse on a continuous time axis, and three output neurons representing the pulse types. The MATLAB function `vec2ind` was employed to inversely normalize and categorize the output neurons. For the $2\pi\alpha$ dataset, the classification results were defined as follows.

$$\alpha_1 = \begin{matrix} 1 \\ 0 \\ 0 \end{matrix}, \quad \alpha_2 = \begin{matrix} 0 \\ 1 \\ 0 \end{matrix}, \quad \alpha_3 = \begin{matrix} 0 \\ 0 \\ 1 \end{matrix}.$$

Whereas for the $2\pi\beta$ dataset, the classification results were defined as follows.

$$\beta_1 = \begin{matrix} 1 \\ 0 \\ 0 \end{matrix}, \quad \beta_2 = \begin{matrix} 0 \\ 1 \\ 0 \end{matrix}, \quad \beta_3 = \begin{matrix} 0 \\ 0 \\ 1 \end{matrix}.$$

A sigmoid function was used as the activation function for our back-propagation neural network. This function maps the weighted sum of the neurons, x , to a value between 0 and 1, effectively capturing the nonlinearity of the input signal.

$$f(x) = \frac{1}{1+e^{-x}}. \quad (1)$$

The performance of our back-propagation neural network was evaluated using mean square error (MSE), which measures how well the model's prediction \hat{Y} matches the true label Y . Specifically, MSE can be applied to both linear regression and simple classification problems. It is expressed as follows.

$$MSE = \frac{1}{n} \sum_{i=0}^n (Y_i - \widehat{Y}_i)^2. \quad (2)$$

Four BP neural network models with varying numbers of hidden layers and neurons were analyzed. The ideal count of hidden layers and neurons often lacks a definitive benchmark and is usually identified through experimentation. Although more hidden layers and neurons can enhance the model's fitting capacity, they may also lead to overfitting and pose challenges during training. Models 1 and 2 incorporate a single hidden layer, whereas Models 3 and 4 encompass two hidden layers. The number of neurons in each hidden layer was adjusted to assess its impact on prediction outcomes. The specifications of the network structure are listed in Table 3 and are further elaborated upon in the Results section. A schematic of the neural network system for Models 1 and 2 is illustrated in Figure 3.

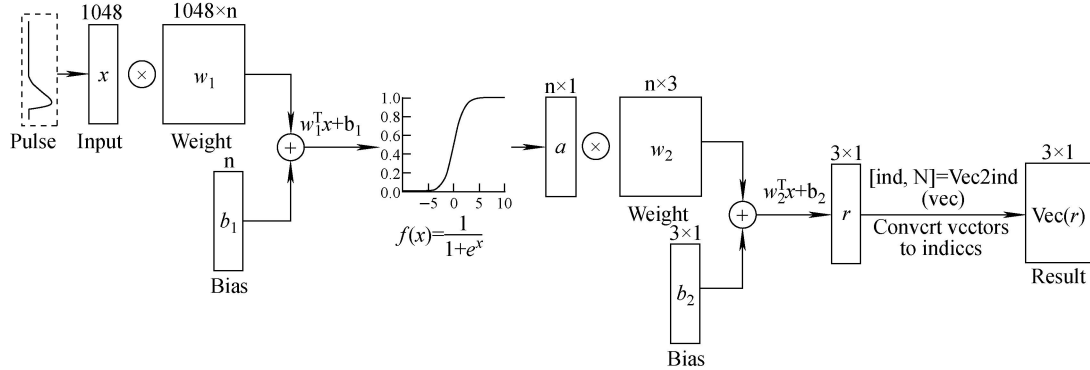


Fig. 3 Block diagram of a BP neural network system with one hidden layer

Based on prior experience, the learning rate, maximum number of iterations, count of validation failures, and minimum threshold of the performance index ε were determined. To satisfy the criteria for performance and gradient, the maximum iteration count should be sufficiently high. Generally, the count of validation failures falls between 10 and 20. Thus, herein, a threshold of $\varepsilon = 1 \times 10^{-6}$ was adopted as the

minimum performance index value.

Table 3 BP neural network structure parameters

Model no.	Input layer; Number of neurons	Output layer; Number of neurons	Hidden layers; Number of layers	Number of neurons in the first hidden layer	Number of neurons in the second hidden layer	Learning rate	Maximum number of iterations	Number of failed validations
Model 1	1048	3	1	10	/	0.01	1000	15
Model 2	1048	3	1	20	/	0.01	1000	15
Model 3	1048	3	2	10	10	0.01	1000	15
Model 4	1048	3	2	20	10	0.01	1000	15

3.2 GA-BP Neural Networks

3.2.1 Principle

Although BP neural networks are widely prevalent, they present challenges such as languid convergence, susceptibility to local minima, and indeterminate network structures. To enhance these attributes, this study employed genetic algorithms for the optimization of the neural networks. Serving as models of biological evolution, genetic algorithms mimic processes of natural selection and genetic inheritance. In the 1960s, Holland introduced a mathematical representation of these algorithms ^[28,29]. This method models the problem-solving approach, akin to biological evolution, essentially encompassing the crossover and mutation ^[30–32] of genetic elements. In this study, genetic algorithms were applied to determine superior initial parameters during forward propagation, which were subsequently refined using back propagation. Figure 4 illustrates a layout of the genetic algorithm-enhanced back-propagation (GA-BP) neural network. Once the structure of the BP neural network was confirmed, its weight and bias parameters were transcribed as elements of chromosomes within the genetic realm. This step enabled the creation of an initial chromosome assembly. Each chromosome was subsequently translated back into a neural network, where its output and error metrics were discerned through forward computations and back-propagation using training datasets. Subsequently, fitness scores for every chromosome were assessed based on the error metrics or alternative measures. An apt fitness function was then engaged to evaluate the viability of each chromosome in the collective. A selection of the most promising chromosomes, as determined by their fitness scores, was advanced to the succeeding generation. Before assembling a new generation, crossover and mutation procedures augmented the genetic diversity of the group. Following a set number of cycles, the chromosome with the foremost fitness score was adopted as the concluding outcome. The processes of population initialization, chromosome inheritance, crossover, and mutation are depicted in Figure 5.

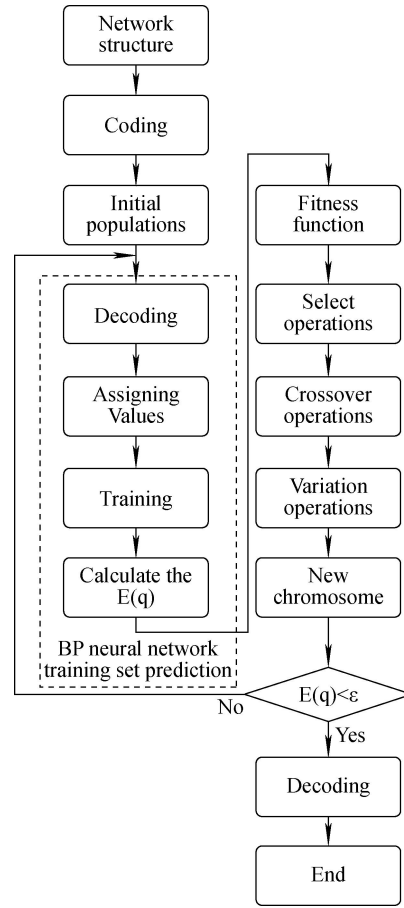


Fig. 4 Schematic of a genetic algorithm-based neural network (GA-BP)

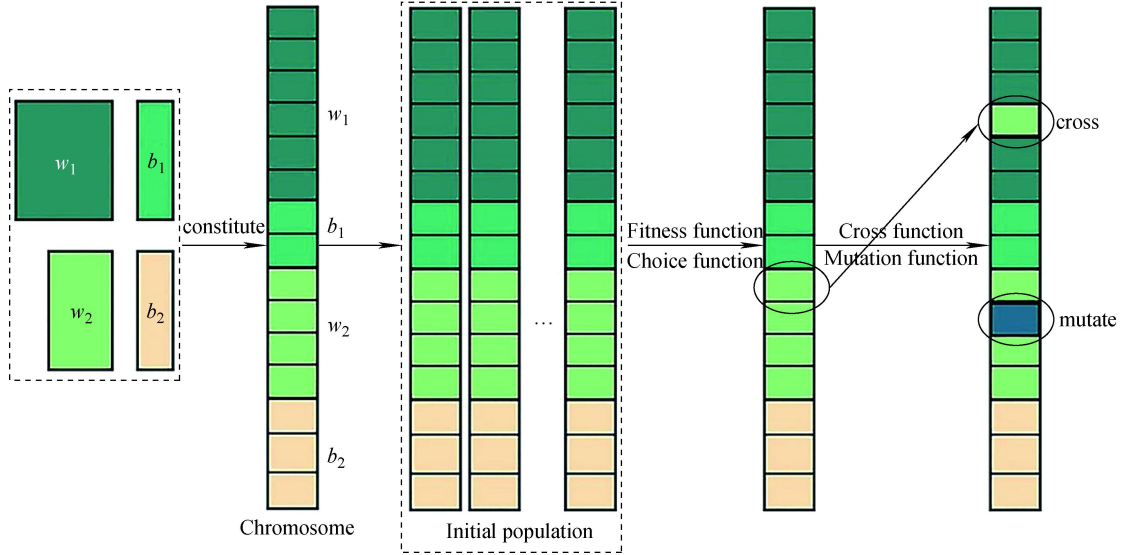


Fig. 5 Population initialization and chromosome inheritance, crossover, and mutation processes in genetic algorithms

3.2.2 Network structure and parameters

An identical GA-BP neural network was employed to train with the $2\pi\alpha$ and $2\pi\beta$ measurement datasets. Parameters from Model 1 of the BP neural network informed the configuration of the input layer, hidden layer, output layer, activation function, performance evaluation index, learning rate, maximum iteration count, and number of

validation failures. For the genetic algorithm, the parameters encompassed population size, number of genetic generations, and the choices of an appropriate fitness function, selection function, and crossover function.

Three distinct GA-BP neural network structures, each with varied genetic algorithm parameters, are crafted as detailed in Table 4. Models 5 and 6 differ in terms of their number of generations, whereas Models 5 and 7 differ in terms of their population size. A detailed comparison of these models, rooted in their training outcomes, is elaborated upon in Section 4.

Table 4 GA-BP neural network structure and genetic algorithm parameters

Model no.	Input layer; Number of neurons	Output layer; Number of neurons	Hidden layers; Number of layers	Number of neurons in hidden layer	Population size	Genetic generation
Model 5	1048	3	1	10	4	10
Model 6	1048	3	1	10	4	15
Model 7	1048	3	1	10	8	10

Genetic algorithm functions were implemented using MATLAB's Gaot toolbox. The fitness function was `gabpEval`, selection function was `normGeomSelect` (geometric ranking selection), crossover function was `arithXover` (arithmetic crossover), and mutation function was `nonUnifMutation` (non-uniform mutation). Default parameters were maintained for these functions.

4. Result

Herein, the energy spectrum measurements of plane sources were obtained and the two ANNs methods for identifying $2\pi\alpha$ and $2\pi\beta$ particles were compared.

4.1 Results of energy spectrum measurements

The energy spectra of the four-plane sources were measured using the experimental equipment described in this study.

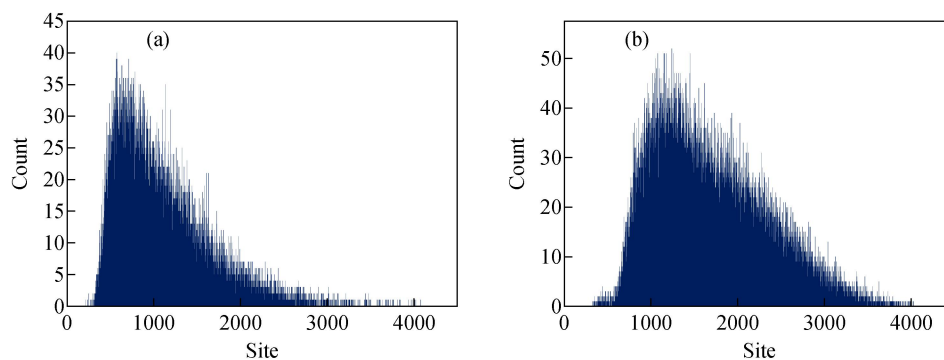


Fig. 6 Energy spectra of (a) ^{238}Pu and (b) ^{241}Am with a cumulative measurement time of approximately 10 s.

The energy spectra of ^{238}Pu and ^{241}Am used in this study are shown in Figure 6. The proportional counter exhibited a low energy resolution, and the particle energies of ^{238}Pu and ^{241}Am ranged from 300 to 2500 and from 600 to 3500 channel sites, respectively. Nuclide particles could not be identified in the channel address range of 600–2500. Identification was possible with single-nuclide measurements but not with mixed measurements.

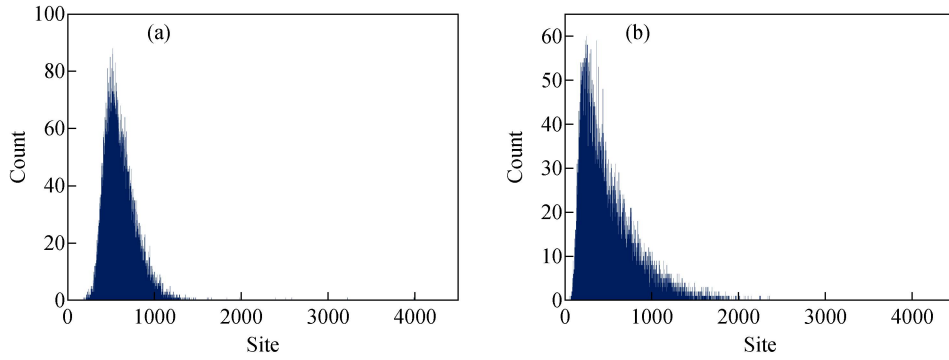


Fig. 7 Energy spectra of (a) ^{204}Tl and (b) ^{90}Sr with a cumulative measurement time of approximately 10 s.

Figure 7 shows the energy spectra of the two-plane sources. The spectra overlapped considerably and were difficult to analyze. Only a few particles that were not in the energy-crossing region were identified.

4.2 Results of BP neural network training.

Four BP neural network models were trained using randomized data arrangements from $2\pi\alpha$ and $2\pi\beta$ experimental datasets. The results for the four network structures are presented in Table 5.

Table 5 Pulse shape discrimination results for $2\pi\alpha$ and $2\pi\beta$ particles using BP neural network model

Model No.	Type	Accuracy (%)		Linear regression coefficient R			Training duration (h)
		Trainin g set	Verificatio n set	Training set	Verificati on set	Total dataset	
Model 1	$2\pi\alpha$	98.46	98.25	0.95591	0.94279	0.95148	1.67
Model 2	$2\pi\alpha$	98.70	98.29	0.96122	0.94583	0.95599	11.20
Model 3	$2\pi\alpha$	99.46	98.25	0.99738	0.97479	0.99165	13.88
Model 4	$2\pi\alpha$	99.56	98.42	0.99961	0.98563	0.99456	8.07
Model 1	$2\pi\beta$	94.40	93.00	0.91953	0.91611	0.91504	5.42
Model 2	$2\pi\beta$	94.77	93.56	0.92117	0.91127	0.91476	36.28
Model 3	$2\pi\beta$	95.12	93.81	0.93741	0.91590	0.93030	5.88
Model 4	$2\pi\beta$	95.19	94.42	0.94181	0.91497	0.93666	32.67

A comparison of pulse shape discrimination results for $2\pi\alpha$ and $2\pi\beta$ particles using four BP neural network models reveals that Model 4 exhibited the highest accuracy for the training and validation sets, as well as the linear regression coefficient. The confusion matrix results of the $2\pi\alpha$ particle training and validation sets of Model 4 are shown in Figure 8, and the confusion matrix results of the $2\pi\beta$ particle training and validation sets of Model 4 are shown in Figure 9.

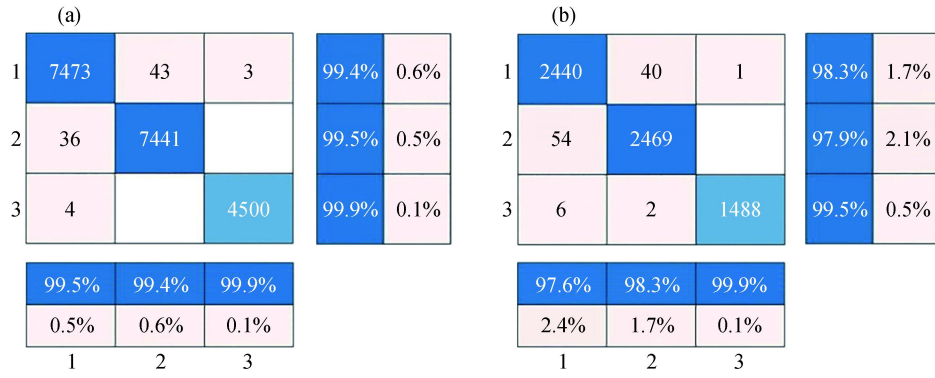


Fig. 8 Confusion matrix for $2\pi\alpha$ dataset using BP neural network (Model 4): (a) training dataset and (b) validation dataset. The matrix has three rows and three columns; each row represents the classification results of true values for α_1 , α_2 , and α_3 datasets, and each column represents the classification results of predicted values for α_1 , α_2 , and α_3 datasets. Here, 1, 2, and 3 denote α_1 , α_2 , and α_3 datasets, respectively.

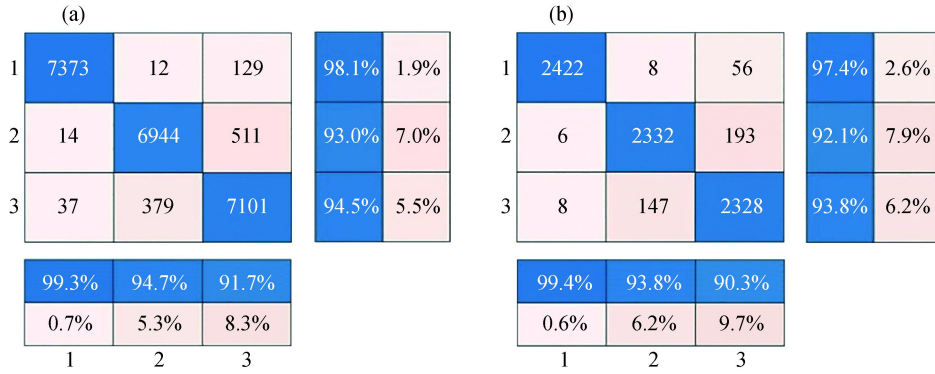


Fig. 9 Confusion matrix for $2\pi\beta$ dataset using BP neural network (Model 4): (a) training dataset and (b) validation dataset. The matrix has three rows and three columns; the rows and columns represent the true value classification results and predicted value classification results, respectively. Here, 1, 2, and 3 denote β_1 , β_2 , and β_3 datasets, respectively.

4.3 Results of GA-BP neural network training.

Three GA-BP models were employed to train $2\pi\alpha$ and $2\pi\beta$ experimental datasets. The data arrangements for both datasets were randomized. The results for the three network structures are presented in Table 6.

Table 6 Pulse shape discrimination results for $2\pi\alpha$ and $2\pi\beta$ particles using GA-BP neural network model

Model No.	Type	Accuracy (%)		Linear regression coefficient R			Training duration (h)
		Training set	Verification set	Training set	Verification set	Total dataset	
Model 5	$2\pi\alpha$	96.13	95.66	0.94716	0.93453	0.94336	15.05
Model 6	$2\pi\alpha$	97.11	96.09	0.96049	0.94532	0.95471	18.07
Model 7	$2\pi\alpha$	98.27	97.35	0.96896	0.95561	0.96505	42.07
Model 5	$2\pi\beta$	91.13	90.64	0.88990	0.88433	0.88664	24.13
Model 6	$2\pi\beta$	91.82	90.40	0.90305	0.87136	0.89377	30.05
Model 7	$2\pi\beta$	94.20	91.87	0.93072	0.89286	0.91910	144.05

A comparison of pulse shape discrimination results for $2\pi\alpha$ and $2\pi\beta$ particles using three GA-BP neural network models reveals that Model 7 exhibited the highest

accuracy for the training and validation sets, as well as the linear regression coefficient. The confusion matrix results of the $2\pi\alpha$ particle training and validation sets of Model 7 are shown in Figure 10, and the confusion matrix results of the $2\pi\beta$ particle training and validation sets of Model 7 are shown in Figure 11.

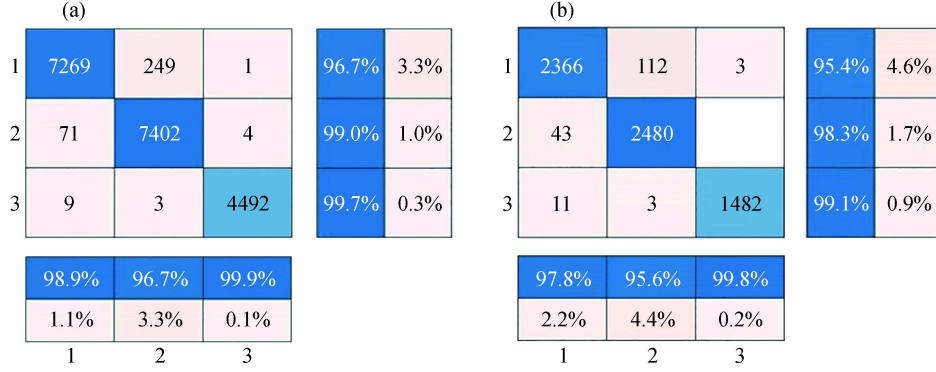


Fig. 10 Confusion matrix for $2\pi\beta$ dataset using GA-BP neural network (Model 7): (a) training dataset and (b) validation dataset. The matrix has three rows and three columns; the rows and columns represent the true value classification results and predicted value classification results, respectively. Here, 1, 2, and 3 denote α_1 , α_2 , and α_3 datasets, respectively.

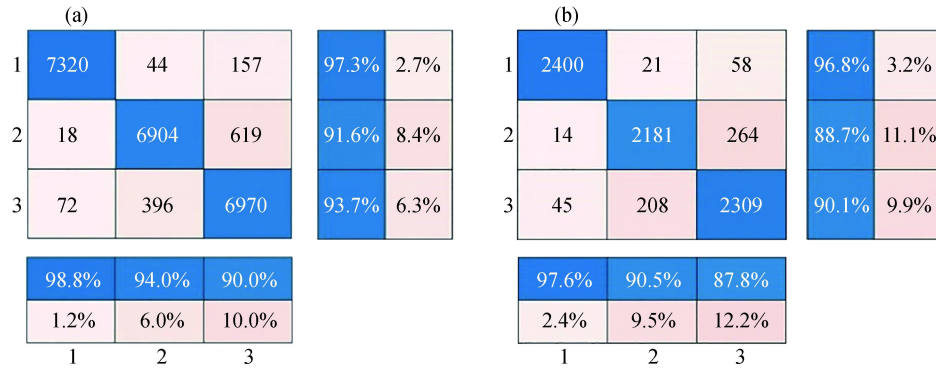


Fig. 11 Confusion matrix for $2\pi\beta$ dataset using GA-BP neural network (Model 7): (a) training dataset and (b) validation dataset. The matrix has three rows and three columns; the rows and columns represent the true value classification results and predicted value classification results, respectively. Here, 1, 2, and 3 denote β_1 , β_2 , and β_3 datasets, respectively.

5. Discussion

The energy spectrum measurements detailed in Section 4.1 indicate that relying solely on energy analysis techniques is an ineffective strategy for distinguishing between $2\pi\alpha$ and $2\pi\beta$ particles. To accurately differentiate between pulse signals, the energy analysis should be combined with information on the signal timing and frequency. Nonetheless, merging these methods necessitates more resources and time, thus compromising efficiency.

Evidently from the results showcased in Tables 5 and 6, several BP neural network models generally surpass the GA-BP neural network models in terms of accuracy rates and linear regression coefficients. Importantly, the BP neural network models not only demonstrated superior outcomes but also necessitated shorter training durations, particularly when the computing resources (CPU) were relatively poor.

The performance in distinguishing $2\pi\alpha$ particles is illustrated in the confusion matrices depicted in Figures 8 and 10. Figures 8(a) and (b) highlight Model 4's high

prediction accuracy, as all three $2\pi\alpha$ signals surpassed 99%. Conversely, the accuracy rates for training and validation sets using Model 7 were somewhat subpar. Figure 10(b) indicates that 112 pulse shapes from the α_1 set were incorrectly identified as α_2 ; consequently, the accuracy rate was approximately 95.5%. This suggests that Model 7 is more prone to misclassifying α_1 signals as α_2 . Hence, the BP neural networks were significantly more effective in distinguishing $2\pi\alpha$ particles.

With respect to the discrimination of $2\pi\beta$ particles, the corresponding confusion matrices are outlined in Figures 9 and 11. For β_1 , both neural network algorithms showcased exceptional classification, with Figure 9(b) projecting a 99.4% accuracy for the β_1 validation set. An analysis of the predictive classifications in the matrix to understand the suboptimal discrimination shows that the predicted outcomes for β_1 and β_2 datasets are commendable, thereby discounting the prospect of a high detector background signal. Thus, the poor classification of β_2 and β_3 datasets can be attributed to the resemblance of pulse shapes in the β_2 dataset to those in the β_3 dataset, thus leading to decreased accuracy for the overall dataset. The introduction of α -nuclide (^{241}Am) contamination to the detector made it more likely to misidentify contaminated signals as belonging to the β_2 dataset. Observations of the β_3 set via an oscilloscope revealed that signals in the β_3 dataset mainly consisted of low-energy pulses, suggesting that the pulse signals of α at a high voltage of 2800 V are resemblance to the signals of β of low energy. Future research could focus on establishing an apt energy threshold to filter these low-energy signals using a digital acquisition card, followed by estimating the $2\pi\beta$ surface emission rate post a minor energy adjustment.

6. Conclusion

In this study, two neural network-driven pulse shape discrimination methods were developed to address the challenges inherent in traditional $2\pi\alpha$ and $2\pi\beta$ particle surface emission rate measurements. These techniques were assessed over six distinct datasets, where four were under standard operation and two simulated contamination scenarios. Various network architectures and parameters were explored for both methodologies, with the optimal parameters being determined based on empirical findings.

The results demonstrated the potential of neural network algorithms in distinguishing particle types in radio-nuclide-contaminated detectors. Following successful classification, surface emission rate measurements can be derived from a statistical analysis, thus enabling more detailed nuclide mixture assessments. However, a notable challenge emerged: the absence of a universally accepted criterion for tuning neural network algorithm parameters. This necessitated adjustments based on hands-on experiments or expert recommendations.

When comparing the two algorithms, the BP neural network exhibited superior efficiency in the training process than the GA-BP neural network. The intricacies associated with the parameter requirements of the latter may account for this discrepancy. If these parameters are not set properly, then it could initiate an exhaustive series of iterative computations, potentially causing the network to prematurely converge or become ensnared in a local optimum.

For more accurate $2\pi\beta$ particle surface emission rate assessments and nuclide

identification, we suggest an adjustment to the energy threshold of the digital acquisition system. This would ensure the extraction of a more refined training dataset.

In summation, the study highlighted the efficacy of neural networks in $2\pi\alpha$ and $2\pi\beta$ pulse shape discrimination and subsequent classification for particle surface emission rate evaluations. This approach eliminates the need for signal preprocessing and significantly enhances pulse-shape differentiation efficiency. Furthermore, its inherent adaptability and scalability hint at its potential applicability in other α and β detection mechanisms.

References

- [1] International Organization for Standards, *Reference sources — calibration of surface contamination monitors — alpha-, beta- and photon emitters*. (Geneva, Switzerland, 2018).
- [2] International Organization for Standards, *Measurement of radioactivity — Measurement and evaluation of surface contamination*. (Geneva, Switzerland, 2016).
- [3] F. D. Tang, L. F. He, G. K. Zhao et al., *Verification Regulation of Alpha and Beta Surface Contamination Instruments*, (Beijing, China, 2016).
- [4] F. D. Tang, L. F. He, G. C. Liang et al., *Calibration Specification for α 、 β Planes Sources*, (Beijing, China, 2018).
- [5] P. De. Felice, R. Anuradha, J. Bludovsky et al., Supplementary comparison of the measurement of the alpha and beta particle surface emission rates from large area sources (CCRI(II)-S10 LASCE), *Metro.* **59**, 1A (2022). <https://doi.org/10.1088/0026-1394/59/1A/06007>
- [6] J. C. Mostert, A primary standard for the measurement of alpha and beta particle surface emission rate at the National Metrology Institute of South Africa. *Appl. Radiat. Isot.* **66**, 925–928 (2008). <https://doi.org/10.1016/j.apradiso.2008.02.059>
- [7] S. H. Hwang, J. M. Lee, K. B. Lee et al., Development of a windowless multi-wire proportional chamber (MWPC) counting system for measuring extended-area beta source. *Appl. Radiat. Isot.* **126**, 175–178 (2017). <https://doi.org/10.1016/j.apradiso.2017.01.031>
- [8] J. Zhang, M. Zhang, L. Duan et al., The large-area multi-wire proportional counting system for 2π alpha and beta emission measurement at the NIM China. *Appl. Radiat. Isot.* **134**, 366–369 (2018). <https://doi.org/10.1016/j.apradiso.2017.08.014>
- [9] L. E. King, J. M. Hutchinson, M. P. Unterweger, A new large-area 2π proportional counting system at NIST. *Appl. Radiat. Isot.* **66**, 877–880 (2008). <https://doi.org/10.1016/j.apradiso.2008.02.079>
- [10] D. Savran, B. Löher, M. Miklavc et al., Pulse shape classification in liquid scintillators using the fuzzy c-means algorithm. *Nucl. Instrum. Methods Phys. Res. Sect. A* **624**, 675–683 (2010). <https://doi.org/10.1016/j.nima.2010.09.130>
- [11] G. Liu, M.D. Aspinall, X. Ma et al., An investigation of the digital discrimination of neutrons and γ rays with organic scintillation detectors using an artificial neural network, *Nucl. Instrum. Methods Phys. Res. Sect. A* **607**, 620–628 (2009). <https://doi.org/10.1016/j.nima.2009.06.027>
- [12] R. Jiménez, M. Sánchez, J.A. Gómez et al., Implementation of a neural network for digital pulse shape analysis on a FPGA for on-line identification of heavy ions. *Nucl. Instrum. Methods Phys. Res. Sect. A* **674**, 99–104 (2012). <https://doi.org/10.1016/j.nima.2012.01.034>
- [13] S. Joung, Y. Kim, J. Kim et al., Simultaneous quantitative analysis of ^3H and ^{14}C radionuclides in aqueous samples via artificial neural network with a liquid scintillation counter. *Appl. Radiat. Isot.* **170**, 109593 (2021). <https://doi.org/10.1016/j.apradiso.2021.109593>.

-
- [14] R. Panahi, S. A. H. Fegghi, S. R. Moghandam et al., Simultaneous alpha and gamma discrimination with a phoswich detector using a rise time method and an artificial neural network method. *Appl. Radiat. Isot.* **154**, 108881 (2019). <https://doi.org/10.1016/j.apradiso.2019.108881>
- [15] X. Fabian, G. Baulieu, L. Ducroux et al., Artificial neural networks for neutron/ γ discrimination in the neutron detectors of NEDA, *Nucl. Instrum. Methods Phys. Res. Sect. A* **986**, 164750 (2021). <https://doi.org/10.1016/j.nima.2020.164750>.
- [16] H. Arahmane, E. M. Hamzaoui, Y. B. Maissa et al., Neutron-gamma discrimination method based on blind source separation and machine learning. *Nucl. Sci. Tech.* **32**, 18 (2021). <https://doi.org/10.1007/s41365-021-00850-w>
- [17] H.R. Liu, Z. Zuo, P. Li et al., Anti-noise performance of the pulse coupled neural network applied in discrimination of neutron and gamma-ray. *Nucl. Sci. Tech.* **33**, 75 (2022). <https://doi.org/10.1007/s41365-022-01054-6>
- [18] Z. Zuo, H. R. Liu, Y.C. Yan et al. Adaptability of n- γ discrimination and filtering methods based on plastic scintillation. *Nucl. Sci. Tech.* **32**, 28 (2021). <https://doi.org/10.1007/s41365-021-00865-3>
- [19] C. X. Zhang, S. T. Lin, J. L. Zhao et al., Discrimination of neutrons and γ -rays in liquid scintillator based on Elman neural network. *Chinese Phys. C* **08** 40 (2016). <https://doi.org/10.1088/1674-1137/40/8/086204>
- [20] H. Sahiner, X. Liu, Gamma spectral analysis by artificial neural network coupled with Monte Carlo simulations. *Nucl. Instrum. Methods Phys. Res. Sect. A* **953** 163062 (2020). <https://doi.org/10.1016/j.nima.2019.163062>
- [21] J. Kim, K. T. Lim, J. Kim et al., Quantitative analysis of NaI(Tl) gamma-ray spectrometry using an artificial neural network. *Nucl. Instrum. Methods Phys. Res. Sect. A* **944** 162549 (2019). <https://doi.org/10.1016/j.nima.2019.162549>
- [22] J. P. He, X. B. Tang, P. Gong et al., Spectrometry analysis based on approximation coefficients and deep belief networks. *Nucl. Sci. Tech.* **29**, 69 (2018). <https://doi.org/10.1007/s41365-018-0402-4>
- [23] C. Fu, A. D. Fulvio, S.D. Clarke et al., Artificial neural network algorithms for pulse shape discrimination and recovery of piled-up pulses in organic scintillators. *Ann. Nucl. Energy* **120**, 410–421 (2018). <https://doi.org/10.1016/j.anucene.2018.05.054>.
- [24] A. Regadío, L. Esteban, S. Sánchez, Unfolding using deep learning and its application on pulse height analysis and pile-up management. *Nucl. Instrum. Methods Phys. Res. Sect. A* **1005**, 165403 (2021). <https://doi.org/10.1016/j.nima.2021.165403>.
- [25] X. Ma, H. Huang, Q. Wang et al., Estimation of Gaussian overlapping nuclear pulse parameters based on a deep learning LSTM model. *Nucl. Sci. Tech.* **30**, 171 (2019). <https://doi.org/10.1007/s41365-019-0691-2>
- [26] Y. Liu, J. Zhu, N. Roberts et al., Recovery of saturated signal waveform acquired from high-energy particles with artificial neural networks. *Nucl. Sci. Tech.* **30**, 148 (2019). <https://doi.org/10.1007/s41365-019-0677-0>
- [27] M. Lin, H. Ye, L. J. Xu et al., Test of proportional counter system with effective detective area larger than 1000 cm². *Atomic Energy Science and Technology* **50**, 713–719(2016) (in Chinese). <https://doi.org/10.7538/yzk.2016.50.04.0713>
- [28] O. G. Selfridge, E. L. Rissland, M. A. Arbib, *Adaptive Control of Ill-Defined Systems*. (Springer, Boston, 1984). https://doi.org/10.1007/978-1-4684-8941-5_21
- [29] D. E. Goldberg, J. H. Holland, Genetic algorithms and machine learning. *Machine Learning* **3**, 95–99 (1988). <https://doi.org/10.1007/BF00113892>

-
- [30] Z. Michalewicz, C. Z. Janikow, J. B. Krawczyk, A modified genetic algorithm for optimal control problems. *Comput. Math. Applic.* **23**, 83–94 (1992).
[https://doi.org/10.1016/0898-1221\(92\)90094-X](https://doi.org/10.1016/0898-1221(92)90094-X)
- [31] S. M. Libelli, P. Alba, Adaptive mutation in genetic algorithms. *Soft comput.* **4**, 76–80 (2000).
<https://doi.org/10.1007/s005000000042>
- [32] J. H. Holland, Genetic algorithms and the optimal allocation of trials. *SIAM J. Comput.* **2**, 88–105 (1973). <https://doi.org/10.1137/0202009>